Chapter 6

Tailor-made Synthesis of Lemon-CDs-Curcuminoid based Assemblies with Tunable Cavities for Development of Sustained Drug Delivery System




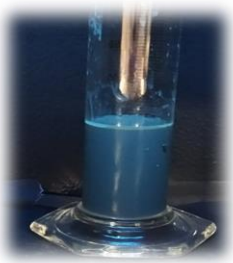


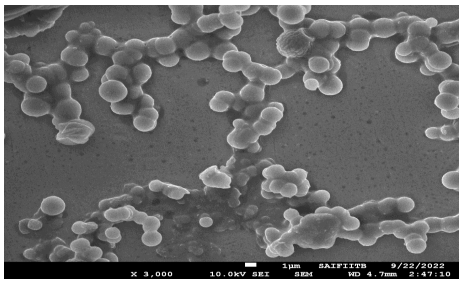

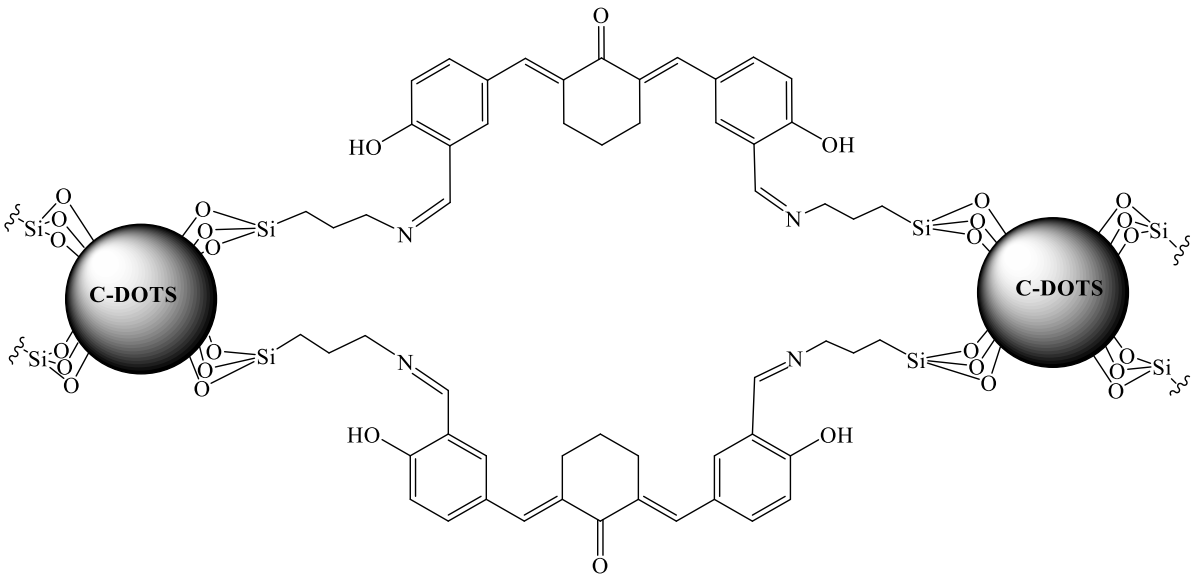

6.1. Introduction

A biocompatible multifunctional nanosystem, also known as a bionanoplatform, intends to develop innovative strategies for combining drug administration, imaging, and cancer therapy functions in a single system. Engineering of multifunctional nanosystems has been encouraged by the development of therapeutic strategies for cancer treatment that demand improved efficacy[1-3].

Many nanomaterials with prospective medicinal applications, particularly drug delivery systems, are now available because of advancements in nanotechnology. Albumin, gelatin, dendrimers, xerogels, polymer nanoparticles (such as Ɛ-caprolactone and polyacrylamide)[4-6], mesoporous silica nanoparticles[6-9], carbon nanomaterials (such as nanotubes and nanohorns)[10-13], and magnetic nanoparticles have all been utilised in drug delivery studies[14-18].

From ancient times, plant-based natural products have been widely utilised as medicines to treat illnesses, and many modern drugs are still predominantly derived from natural sources[19]. Recently, plant-based nanostructures such as carbon dots (CDs) made from natural source such as lemon peel[20-22], lemon juice[22-31], watermelon[32-34] and other materials have drawn attention because they are affordable, renewable, and offer exceptional physicochemical qualities that are ideal for a variety of applications.

Carbon nanoparticles that are discrete, quasi-spherical, and less than 10 nm diameter make up carbon quantum dots. The fluorescent CDs exhibit highly interesting features, including strong, adjustable luminescence, non-toxicity[35], and high photoluminescence (PL) quantum yield values in comparison to typical semiconductor quantum dots[36-38], and many other distinct nanocarbons. CDs are promising candidates for a variety of advanced potential applications, particularly in the field of biological sciences like optical bioimaging[39], cell labelling[40], metal ion sensing[41], and drug delivery[42], due to their higher functionality, hydrophilicity, excellent biocompatibility, and high photostability[43].

Engineering of multifunctional nanosystems has been encouraged by the development of therapeutic strategies for cancer treatment that demand improved efficacy. The creation of CDs typically involves two methods, such as top-down and bottom-up[44]. The use of a number of techniques or technologies, including acid oxidation,[45,46] laser ablation[47], electrochemical

synthesis[48], pyrolysis or carbonization of organic precursors,[49,50] as well as preparations on solid supports, has been utilized[51,52].

It has generally been demonstrated that a thermal preparation yields a larger quantum yield than other conventional techniques. Lot of research has been done to determine which precursors will produce a larger quantum yield, but the outcomes have been less clear[53,54].

In aqueous medium and other solvents, bare CDs without surface functionalization or passivation often produce relatively weak emissions[55]. The surface of CDs is favourable for surface functionalization and/or passivation with organic moieties or polymers due to the abundance of carboxyl groups or hydroxyl groups[56,57]. This has received widespread acceptance as a successful strategy for increasing the quantum yield of CDs. To achieve this goal, doping[58] and co-doping[59] with boron, nitrogen, sulphur, silicon, or phosphorus are other options. CDs gives high emission in the visible spectrum or even into the near infrared spectrum by surface passivation or doping.

In principle, functional groups on CDs produce structural flaws and mid gap states that facilitate transitions between $\pi^* \rightarrow$midgap $\rightarrow \pi$ and enhance the red components on their PL spectra[60]. An intriguing study found that the band gap rapidly decreased in a series of CDs with similar size distribution and graphitization level as surface oxidation increased. This resulted in a noticeable red shift from 440 to 625 nm[61].

One of the most common methods for nanoparticle surface modification is silica coating with the help of organo-silane self-assembly[62-67]. The creation of a Si-O-Si connection between the surface and the silanol groups is the first step in the self-assembly of organo-silanes[62]. Also, the other end of silane molecule has a broad extension of useful chemical functional groups that allows for flexible customization of the surface for various applications[64]. This coating approach enables the creation of strong hybrid nanocomposites with a cross-linked silica shell to shield the core nanoparticles from the outside environment[68]. Due to its amino terminal group, water-soluble nature, and ability to form a covalently bonded self-assembled monolayer on a variety of substrates, 3-(aminopropyl)triethoxysilane (APTES), a versatile organo-silane used in silica coating, has been widely adopted by the biotechnology industry[69,70].

Using citric acid as the carbon source, Rao et. al. produced CDs-NH_2 by a hydrothermal approach, and then, through a silylation reaction, they covered CDs-NH_2 in a silica shell using

tetraethyl orthosilicate (TEOS) and 3-aminopropyl triethoxysilane (APTES). This modification technique minimises particle aggregation and non-specific binding while producing a favourable balance between inert and active functional groups. Additionally, it adds many amino groups to the surface of CDs, allowing for covalent conjugation with CdTe quantum dots that have undergone thioglycolic acid modification via the EDC/NHS coupling procedure. Additionally, they employed this combination as a ratiometric probe for detecting Cu^{2+} in samples of spiked fruits and vegetables[71].

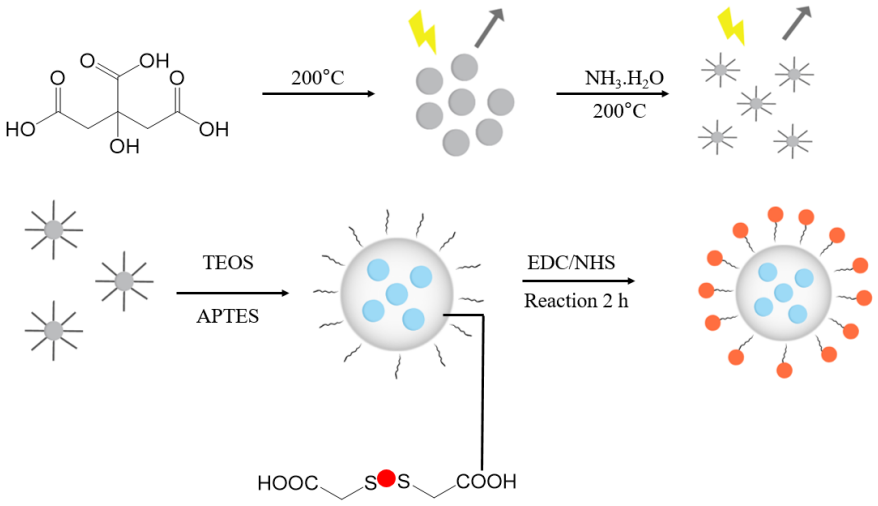

Figure. 6.1. Illustration of the procedure for preparation of the core-satellite C-dot@SiO2@Qdots hybrid spheres[71].

Similarly Niu et. al. also synthesized CDs-NH_2 by a silylation procedure from alanine and histidine as the raw materials and APTES as the modifying reagent. Further they coupled the CDs with AuNCs (nanocluster) through silanization reaction to build a detection system based on inner filter effect (IFE). The resultant CDs were used to detect Cd^{2+} and l-ascorbic acid (AA)[72].

The successful development of detection of metal ions in non-biological system gives the inspiration to use this modified CDs in detection of metals in biological system. For improving the fluorescence detection of extracellular Cu^{2+} in rat brain, Lin et. al. developed a unique silica-coated carbon dots (CDs) based fluorescence platform. The CDs were developed from citric acid based carbon source and functionalized with APTES for fluorescent enhancement. The freshly prepared probe (3.33% APTES-0.9 mg/ml CDs probe) exhibits a synergistic

amplification effect of CDs and APTES on enhancing the fluorescence signal of Cu^{2+} detection using fluorescent self-quenching[73] (figure 6.2).

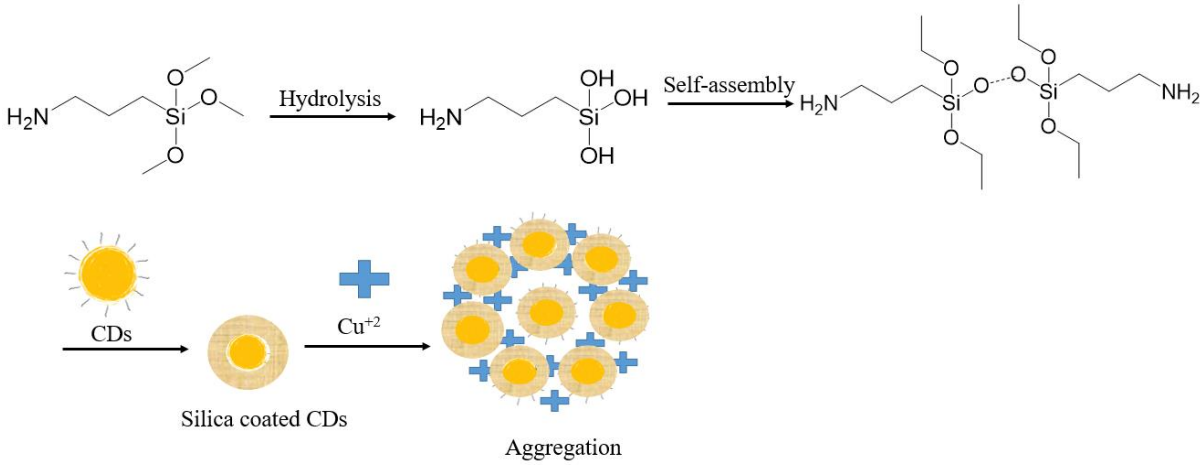

Figure. 6.2. Preparation, principle of Cu^{2+}-induced close proximity, model structure of fluorescent silica coated CDs-based probe.[73]

The detection property of CDs further led to development of a naosensor for organic molecule as well. An endocrine-disrupting organic compound called bisphenol A (BPA), which is prevalent in food packaging, was detected by Liu et. al. The CDs were created utilising a pyrolysis decomposition method employing anhydrous citric acid and N-(β-aminoethyl)-γ-aminopropylmethyldimethoxysilane (AEAPMS) as the precursor source. The nanomaterial was specifically created using molecular imprinting technique (MIT) and in situ hydrothermal synthesis. Molecular imprinted polymer coated CDs (MIP-coated CDs) were created by sol-gel synthesis with a BPA template where BPA binding sites for recognition were created using TEOS and APTES. The researcher developed a straightforward, highly specific BPA nanosensor with nonspecific detection of interfering ions and phenolic compounds and a consistent concentration sensitivity of 100 nM to 4200 nM. This sensing mechanism of nanosensor was based on the fluorescence quenching of CDs[74] (figure 6.4).

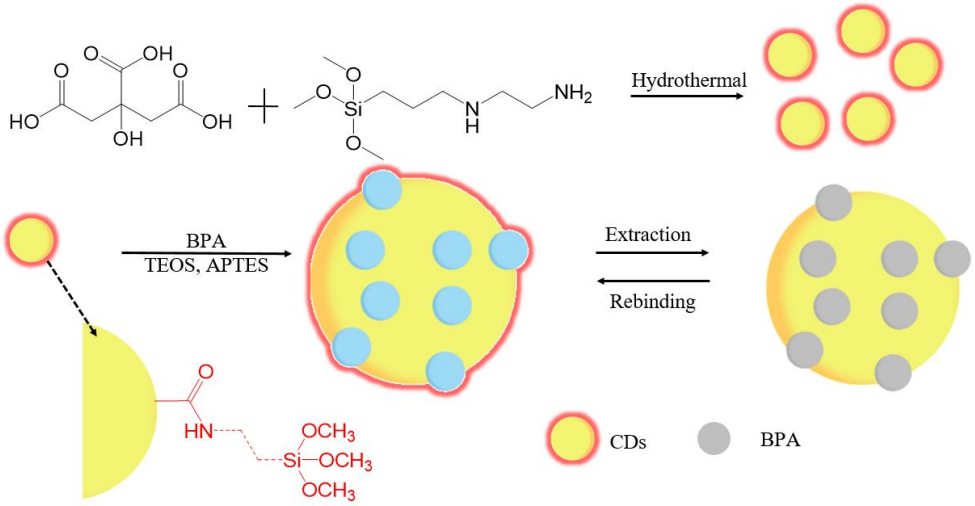

Figure. 6.4. Synthesis of molecularly imprinted polymers coated carbon dots for fluorescent detection of bisphenol A.[74]

The similar investigation was also reported by Yang et. al. They developed the CDs as a sensor for detecting the antibiotic tetracyclin (TC). Citric acid and urea were used as precursors for the hydrothermal synthesis to produce nitrogen-doped CDs, and a modified inverse microemulsion system (cyclohexane/n-hexanol/Triton X-100/water/CDs) was then used to encapsulate the CDs by polymerizing TEOS and APTES. The nanostructure MIP@CDs (molecular imprinted polymer coated CDs) was then created by adding the analyte as a template and washing it away. According to the results, TC is physically adsorbed on the MIP@CDs and has a concentration-dependent quenching effect on the synchronous fluorescence spectra. This work, produced an enhanced theragnostic device for nanomedical applications, which opens up a new potential use for CDs when paired with various nanomaterials[75].

To address the capability of CDs as nanocarrier to deliver the chemotherapeutic drug Kang et. al. developed CDs hollow mesoporous organo-silica nanocarriers (C-hMOSs). It was prepared using a surfactant-template method and precipitation reaction in the presence of hexadecytrimetyl ammonium bromide (CTAB). Hydroxyapatite (HA) nanoparticles, which were used as a core template to build a hollow structure, were created via the precipitation reaction. The core template nanoparticles were coated with a silica structure made by a modified base-catalysed sol-gel technique in order to create the non-hollow & mesoporous nanoparticles. This was accomplished by polymerizing TEOS and APTES. The non-hollow nanoparticles were heated to 400 °C to produce the fluorescent CDs, and the core was

subsequently removed using an acid etching procedure to create a hollow-cored structure. The HeLa cancer cell line was cultured with various concentrations of the DOX-loaded nanoparticles to confirm the theragnostic properties of the nanocarrier. The nanocarrier displayed a fluorescent signal around the tumour, initiated DNA fragmentation, and inhibited tumour growth[76].

A nanocarrier was developed by Shirani et. al. for drug delivery and bioimaging. In a nutshell, the synthesis involved obtaining CDs from glucose and L-aspartic acid by the pyrolysis pathway. Next, with help from CTAB and TEOS, the solgel method was used to create mesosilica-coated CDs (MSCDs). Eventually, APTES was used to add amine groups to the surface of nanoparticle. The MSCDs were then loaded with the anticancer agent epipodophyllotoxin (ETO) and conjugated with β-cyclodextrin (CβCD) through an N-(3-dimethylaminopropyl)-N-ethylcarbodiimide hydrochloride (EDC)/N-hydroxysuccinimide (NHS) reaction to form an amide linkage. This provided multifunctional drug delivery and imaging capabilities. The nanocarrier exhibited pH triggered drug release in acidic microenvironment of HeLa and Hep2 cell lines[77].

6.2. Experimental Section

6.2.1. Materials

The chemicals and solvents used in the preparation of nano-assemblies were of analytical grade. They were purchased from Sigma-Aldrich, Merck and used without further purification.

6.2.2. Synthesis of LCDs-NH_2

In order to synthesize LCDs-NH_2, we primarily synthesized LCDs from Lemon Juice. Briefly, in a 100 ml hydrothermal autoclave, 50 ml of filtered fresh lemon juice was added and held at 180 °C for 8 hours. After the reaction was completed, it was cooled to room temperature and filtered using whatman filter paper-41. Then added drop wise 8.14 ml 3-(triethoxysilyl) propan-1-amine (APTES) into the above solution of LCDs. At room temperature, the reaction was stirred for 24 hours. This reaction was slightly exothermic, resulting in a change in the colour of the reaction mixture from brown to black. The reaction mixture was extracted in n-butanol and excess APTES was left in aqueous layer. The extracted organic layer was dried on molecular sieve, the resulting solution was employed in the next step.

FT-IR (KBr disc, cm^{-1}): 3426.32(ν_{-NH}), 2927.09(ν_{-CHas}), 2856.24(ν_{-CHs}), 1676.18($\nu_{-C=O}$), 1640.53($\nu_{-C=C}$), 1041.13(ν_{-Si-C}).

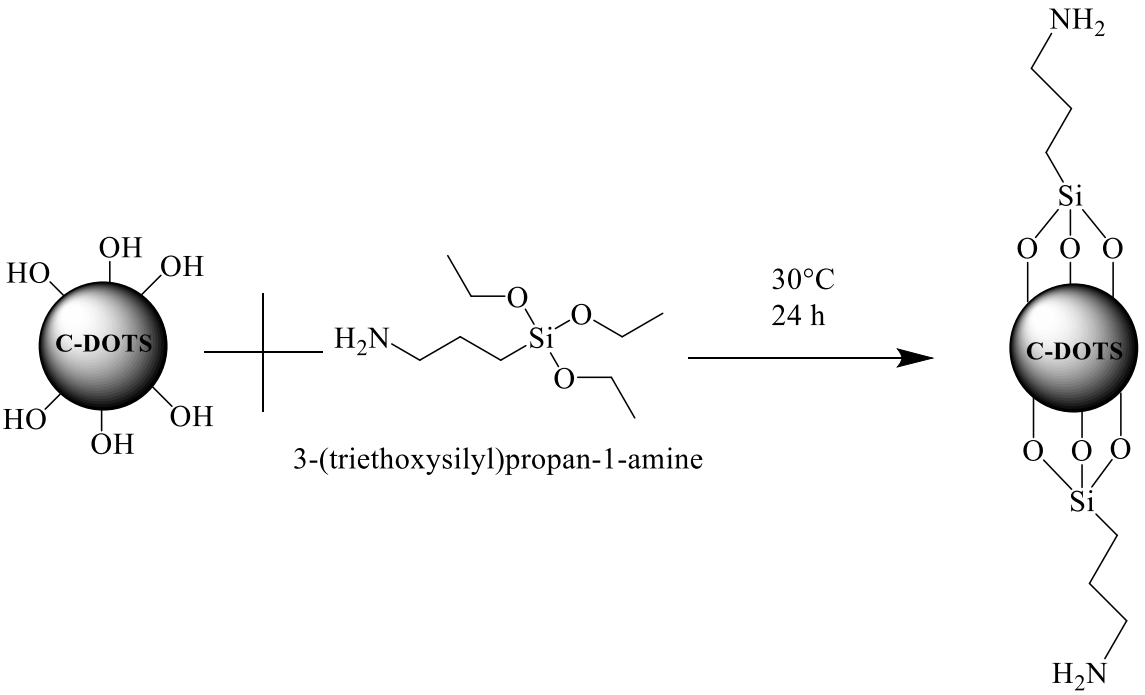

Scheme 6.1. Synthesis of LCDs-NH_2.

6.2.3. Synthesis of nanoassemblies

0.5 g bis-aldehyde was dissolved in 300 ml of n-butanol. Added this solution drop wise in the solution of LCDs-NH_2. The reaction mixture was stirred at room temperature for 24 hours after the addition. The resultant solution was evaporated using a rotary evaporater. The orangish sticky mass was recovered, which was further purified using dichloromethane:methanol :: 99:1 coloumn chromatography. We obtained pure the sticky yellowish brown product which was stored at room temperature for further characterization and use.

FT-IR (KBr disc, cm^{-1}): 1634.70 cm^{-1}($\nu_{-C=N}$)

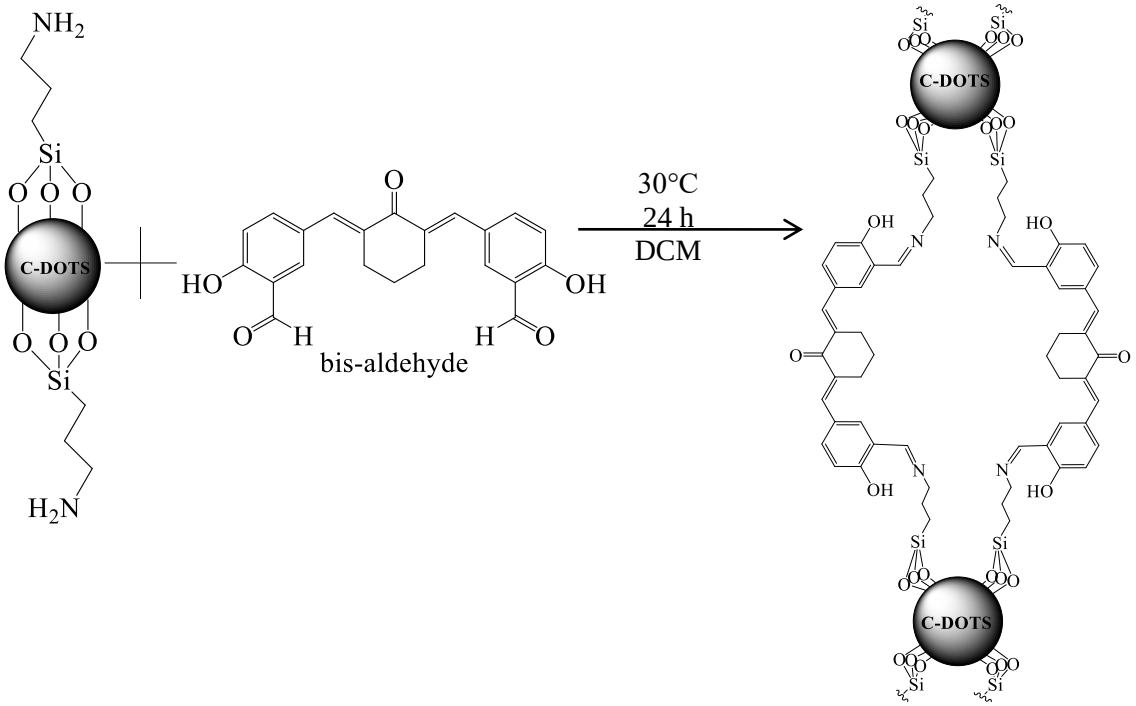

Scheme 6.2. Synthesis of nanoassemblies.

6.2.4. Encapsulation of Methotrexate

Drug methotrexate (MTX) was loaded by kneading method. 1 mg of nanoassemblies and 10 mg of MTX with few drops of dichloromethane, ethanol and water was kneaded. It was allowed to dry for few days. Free flowing powder was obtained.

6.2.5. Calculation of Drug Loading (DL%) of Nanoassembly and Encapsulation Efficiency (EE%) of Methotrexate

The aqueous solution of inclusion complex of 2.0 mg in 2 ml of conductivity water was prepared and placed into 0.1-0.5 kD MWCO, Float-A-Lyser G2, CE, Dialysis Membrane device from Repligen (Spectrum Laboratories), Inc. and subjected to dialysis in 100 ml water for 24 hours at room temperature. The concentration of free drug was determined by withdrawal of 5 ml of release medium and measuring absorption on UV-Vis detection wavelength at 300 nm. The calibration plot for MTX was used to determine the concentration of drug released (Unbound drug) in aqueous medium. The concentration of unbound drug was subtracted from the drug added to the carrier to determine the amount of drug loaded. Using the following formulae, the drug loading (DL) and entrapment efficiency (EE) were estimated in comparison to the standard curve:

$$DL\ (\%) = [(W_{MTX} - W_{Unbound\ MTX}) / W_{MTX\ loaded\ nanoassembly})] \times 100$$

$$EE\ (\%) = [(W_{MTX} - W_{Unbound\ MTX}) / W_{MTX})] \times 100$$

Where,

W_{MTX} = Weight of MTX loaded in nanoassembly

$W_{Unbound\ MTX}$ = Weight of unbound MTX released from inclusion complex

$W_{MTX\ loaded\ nanoassembly}$ = Weight of MTX loaded nanoassembly[37]

6.2.6. Cumulative release of MTX

2 ml aqueous solution of the 1.9 mg of MTX loaded nanoassemblies was dialysed with a 0.1-0.5 kD MWCO, Float-A-Lyzer G2, CE, Dialysis Membrane device from Repligen (Spectrum Laboratories), Inc. in 100 ml of the buffer solution. The study was carried out with PBS (Phosphate buffer solution) of pH 7.4 and PBS of pH 5.5. PBS of pH 7.4 mimics the normal physiological medium and PBS with pH 5.5 simulates the tumour intracellular microenvironment. It was used to evaluate the pH-triggered drug release in vitro. To determine the cumulative drug release, the UV-Vis spectrometer was used to quantify the dialysate at 300 nm during the drug release.

6.2.7. Cytotoxicity assay

The MTT colorimetric assay was performed to evaluate the in vitro cytotoxic activity of nanoassemblies, MTX loaded nanoassemblies and MTX against MCF-7 cell. Firstly, cell line was maintained under appropriate condition environment. MCF-7 cell was harvested in minimum essential medium (MEM) supplemented with 10% Fetal Bovine Serum (FBS) and maintained at 37°C supplemented with 100 I. U./ml Penicillin-Streptomycin, 5 % CO_2 in a CO_2 incubator (Remi, India) with 95% humidity. The cell line obtained from each log-phase of growth were harvested by trypsinization and then resuspended in complete growth medium to give a total of 2×10^4 cells/ml. Then, 200 µl of the cell suspension was seeded into the wells of 96-well plates (Tarson). The plates were incubated overnight in a humidified air atmosphere at 37°C with 5% CO_2. After overnight incubation, the cell was treated with the compounds in concentration range of 0.01-100 µg/ml. The plates were incubated for further 24 h. At the highest concentration of the compounds applied, DMSO accounted for 0.2% of the final concentration. In each plate three control wells (cells without test compounds) and blank wells (the medium with 0.2% DMSO) were kept for cell viability determination. After completion of 24 h incubation time, 10 µl MTT (5 mg/ml), was added to each wells, followed by 4 h of incubation. After incubation, in each well, the culture medium was then replaced with 100 µl of DMSO. After 30 min incubation the plate was shaken for 1 min and then using a microplate reader (Analabs), the absorbance of each well was measured by at 490 nm. For each compound, the concentration that inhibits 50% cell growth has been determined (IC_{50}).

6.3. Results and discussion

LCDs were created using the hydrothermal process over the course of 8 hours at 180 °C using 50 ml of fresh lemon juice. Typically, there are three processes involved in the production of LCDs using the bottom-up approach: Carbonaceous precursors are first pyrolyzed at high temperatures, which causes carbonization and nucleation. Lemon consists of water (88–89 %) and carbohydrates (10%) while protein and fat are both quite low in it. Fibre and sugars including sucrose, fructose, and glucose are typically included in lemon juice. According to the researchers, CDs can be made from any carbohydrate that has C, H, and O in a ratio of 1:2:1, where C and O are in such a form that enables dehydration during hydrothermal processes[78]. During hydrothermal processing, sucrose is hydrolyzed to provide glucose and fructose. The creation of luminous CDs with high quantum yield is thought to include many key steps, one of which is surface passivation[79].

The high water solubility and the abundance of surface functional groups are the main characteristics of LCDs created using this technology, which also account for their numerous variations and applications. However, because of the inherent problems with water-based synthesis, it might not be able to precisely regulate the size distribution and crystallinity of CDs[80].

The surface modification of LCDs is further achieved by drop-wise addition of APTES in the solution of freshly prepared LCDs (scheme 6.1). The colour change from brown to black was observed after the surface modification. On the surface of LCDs, silane and active hydrogen react, resulting in silylation modification. Due to its biocompatibility, nontoxicity, and two different types of functional groups, silane can be used as a silicon shell to enclose two different fluorescent components in order to create multicoloured, harmless fluorescence probes. Moreover, it might increase the specific surface area to improve LCDs dispersion[81]. The modified LCDs-NH_2 is extracted in n-butanol to remove the unreacted APTES. The layer of n-butanol contains the LCDs-NH_2 only which is directly used for developing nanoassemblies.

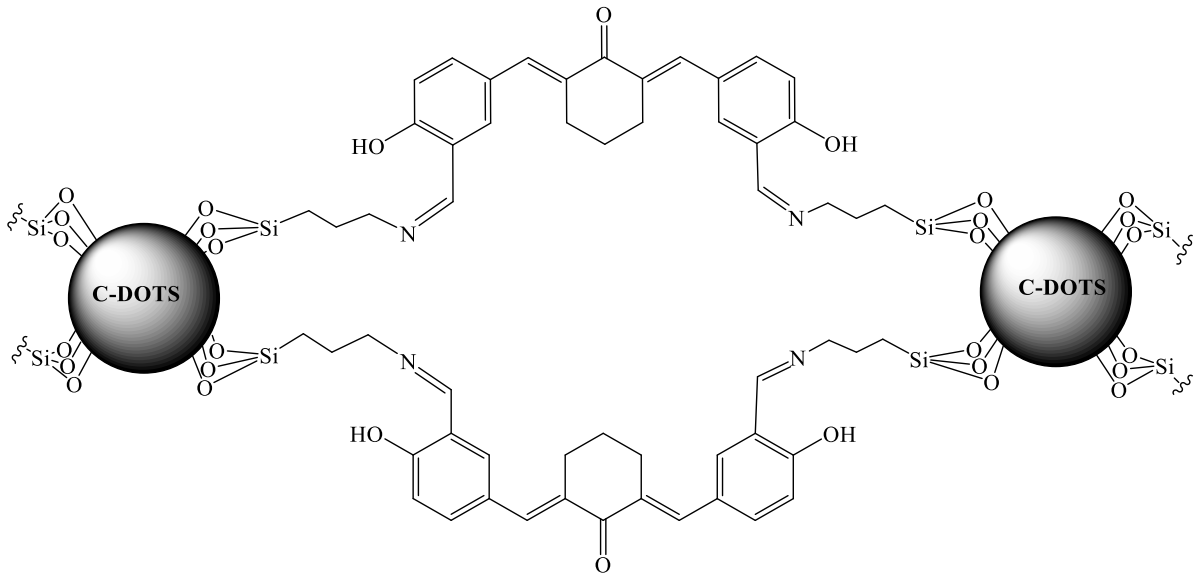

Figure. 6.5. Structure of nano-assembly.

The nano-assembly is developed by using previously synthesized bis-aldehyde in chapter 2 from our group and LCDs-NH_2 at room temperature (scheme 6.2) (figure 6.5). The condensation process between the bis-aldehyde and amine, results in the imine bond formation. The imine formation is followed by a colour change from yellow to orange. The product is further purified by using coloumn chromatography in dichloromethane:methanol :: 99:1.

The LCDs-NH_2 and nanoassemblies are characterized by FT-IR, NMR, DLS, HR-TEM, FEG-SEM, UV-Vis, and Fluorescence spectroscopy.

The FT-IR spectra of LCDs-NH_2 (spectrum 6.1) shows the stretching band of -NH_2 at 3426.32 cm^{-1} and stretching band of C=O at 1676.18cm^{-1}, which revealed the successful grafting of APTES to the LCDs. The two set of bands at 2927.09 cm^{-1} and 2856.24 cm^{-1} corresponds to the asymmetric and symmetric stretch of methylene groups in APTES moiety. The band at 1041.13 cm^{-1} could be attributed to the vibrational stretching of Si–O–C.

Further, in the FT-IR spectrum of nanoassembly (spectrum 6.3), the C=N stretching frequency is observed at 1634.70 cm^{-1}, which suggested the formation of imine bonds. The surface modification is further supported by ^{1}H NMR spectrum of LCDs-NH_2 (spectrum 6.2), which shows the disappearance of peak of active proton around 9.398 ppm in LCDs (chapter 5, spectrum 5.1). After the formation of nanassemblies the peaks of imine proton appears around 8 ppm in the ^{1}H NMR spectrum of nanoassemblies (spectrum 6.4).

The ultraviolet-visible (UV-Vis) absorbance spectra of the nanoassemblies in figure. 6.6 confirm the claim that imine-bond formation is responsible for the assembly of the nanoassemblies, which is in line with the FT-IR results.

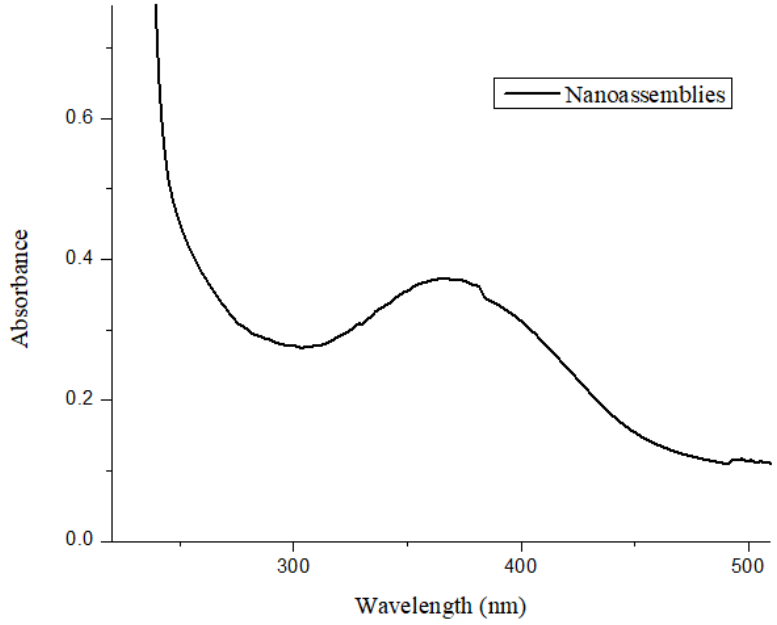

Figure. 6.6. UV-Vis absorption spectrum of nanoassemblies.

Soluble nanoassemblies gave rise to a broad absorbance peak from 280 to 510 nm centred at 367 nm corresponding to n-π * and π–π* transition which corresponds to imine absorption. Carbon dot emission wavelength and size-dependent photoluminescent behaviour are their characteristic features. One of the most remarkable behaviours of carbon dots is PL, both from a theoretical and practical perspective. It was evident from the carbon dot photoluminescent spectra that the PL intensity depends on the dot concentration. This might be because polar group interactions are lessened at low concentrations. At high concentrations, polar functionality plays a role in the formation of agglomeration[82]. The excitation wavelength affects the PL intensity as well. The PL spectrum of nanoassemblies shows a broad emission centered at 451 nm (figure. 6.7).

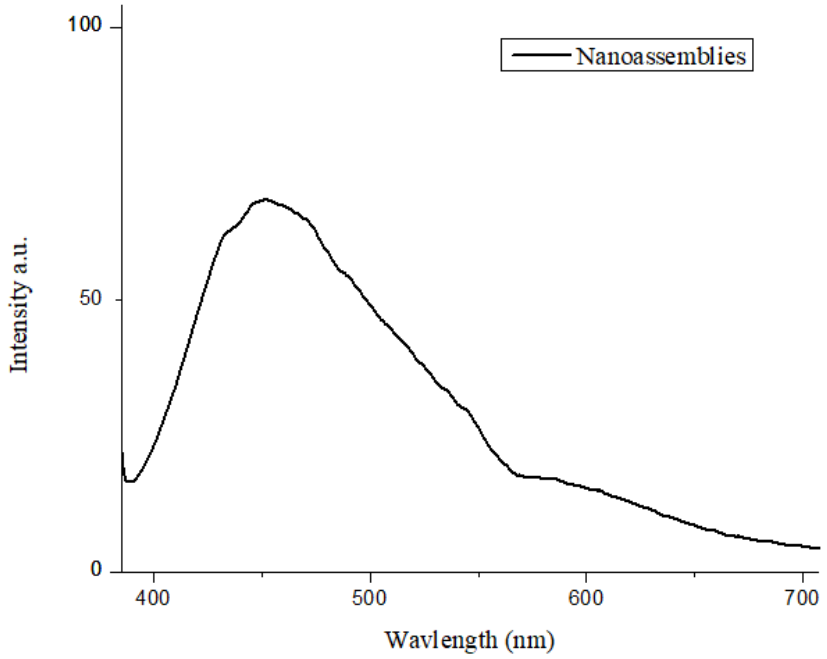

Figure. 6.7. PL (Photoluminescence) spectrum of nanoassemblies.

It is still unclear how PL behaviour of carbon dots works because the mechanism is so complex. The existence of various particle sizes and the distribution of the various surface energy traps of the carbon dots are the likely causes of the PL behaviour. The size variation of the carbon dots is what causes the change in the emission peak position. Due to the quantum confinement effect, which is also present in semiconductor quantum dots, the energy gap widens as the size of the carbon dots decreases and vice versa. Smaller particles are excited at shorter wavelengths while the larger particles are excited at longer wavelengths. The quantity of particles excited at a specific wavelength determines the intensity of PL[82]. Due to the greatest number of particles being excited at that wavelength, the highest PL intensity of nanoassemblies was found at an excitation wavelength of 350 nm. A sequence of emissive traps between π- π* of C=C may form as a result of the presence of different functional groups of the nanoassemblies. When the nanoassemblies are exposed to light at a specific excitation wavelength, a surface energy trap predominates in the emission. As a result, surface defects as well as size effects regulate the PL process. In light of their various potential applications, the PL characteristic of produced nanoassemblies is encouraging. The hydrodynamic diameter of nanoassemblies is 519.5 nm, it is due to the presence of hydrophilic groups such as silanol, imine, and hydroxyl group (figure. 6.8).

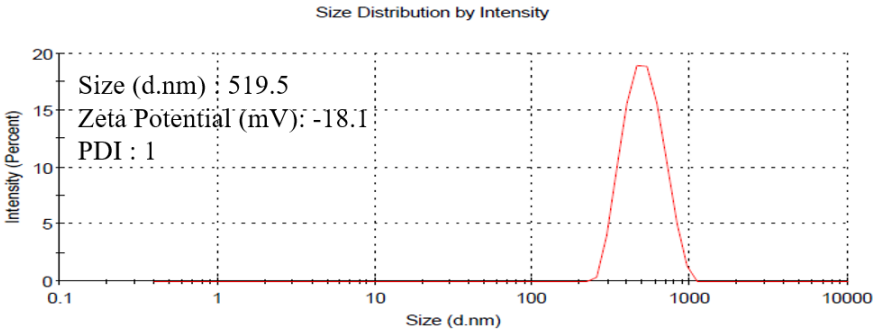

Figure. 6.8. DLS of nanoassemblies.

Using HR-TEM, we looked into the particle size of nanoassemblies. As shown in figure. 6.9, the formation of cross-linked nano-assemblies has the size around 10 nm. The size distribution obtained from the DLS approach (figure. 6.8) is bigger than the particle size obtained from the HR-TEM images because the nanoassemblies aggregate and go through a swelling process in aqueous media[83].

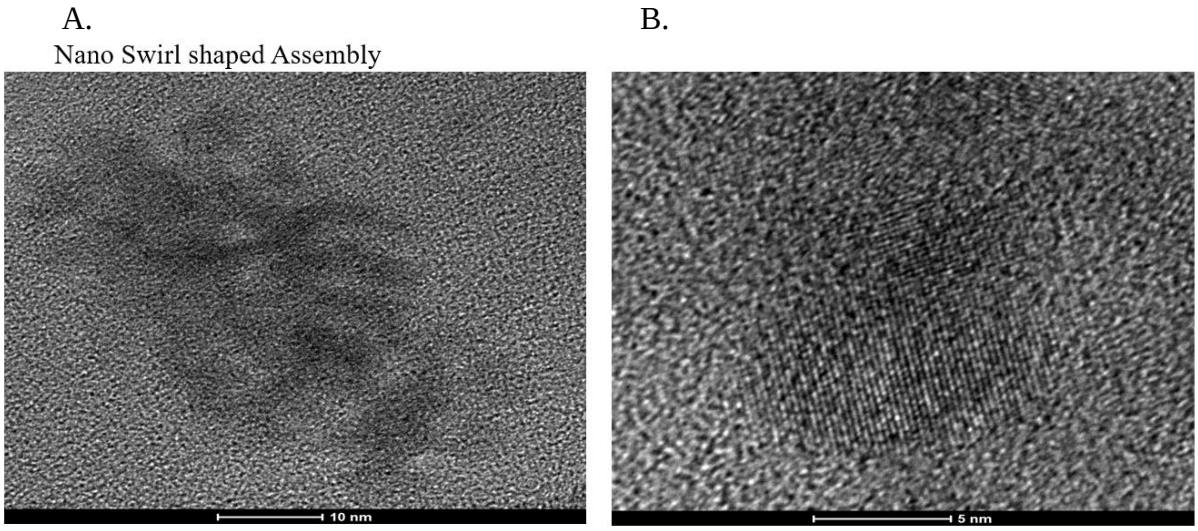

Figure. 6.9. HR-TEM images of nanoassemblies A) scale bar 10 nm, B) scale bar 5 nm.

The surface morphology of nanoassemblies obtained via FEG-SEM are displayed in figure. 6.10. The homogeneity in the shape and size was evident from FEG-SEM images. The size of nanoassemblies falls within the range of preferred sizes for development of efficient drug delivery system[84].

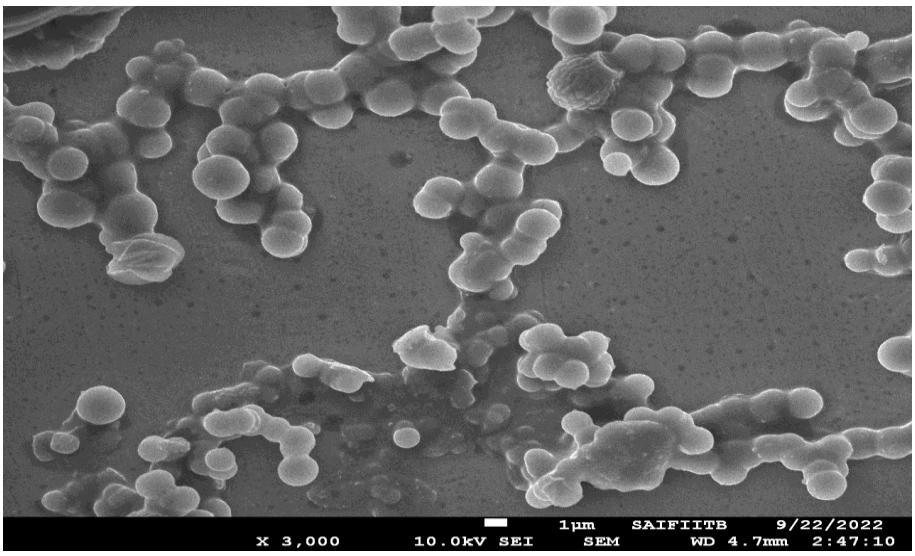

Figure. 6.10. FEG-SEM image at 1 µm.

In order to develop a drug loaded nanoassemblies, MTX was loaded into nanoassemblies via kneading method. The FT-IR spectra of MTX loaded nanoassemblies showed the change in absorption band (spectrum 6.5) compare to their parent molecule (spectrum 6.6). MTX has two carboxylic acid and amine group in its structure which can form hydrogen bond with the phenolic, imine and ketone group of nanoassemblies. The aromatic ring of MTX can form π-π stacking with aromatic ring of nanoassemblies. The binding of methotrexate with nanoassemblies results in blue shift of UV band (figure 6.11),.

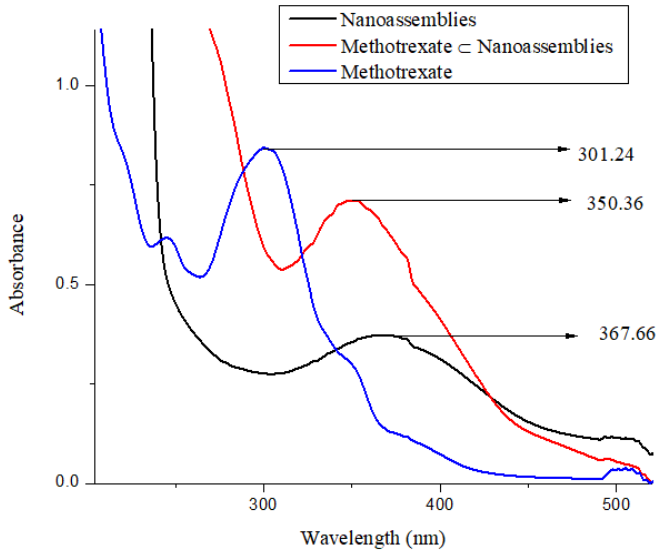

Figure. 6.11. UV-Vis absorption spectra of nanoassemblies, methotrexate loaded nanoassembly and methotrexate.

The aqueous solution of MTX loaded nanoassemblies shows the emission in near NIR region (figure. 6.12). This data suggest that the prepared drug loaded nanoassemblies can be used for in vivo imaging and can be used to track the pathway of its delivery and excretion of nano assemblies.

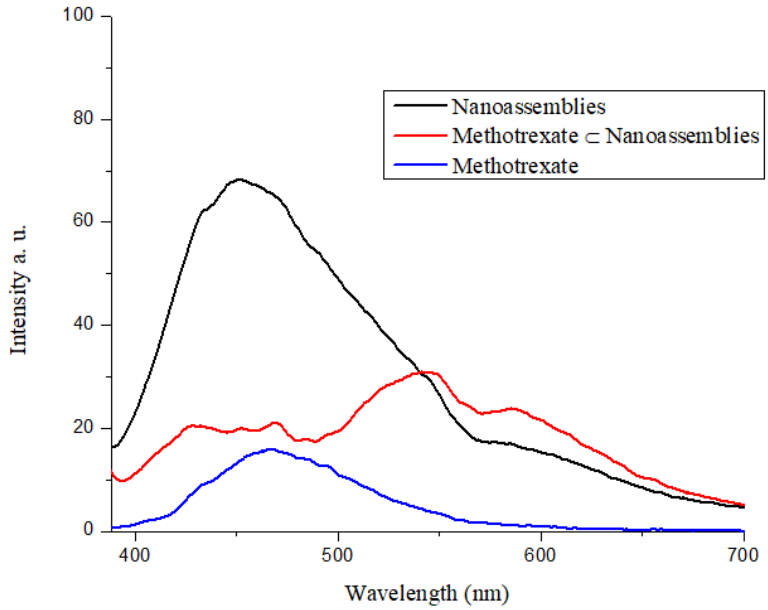

Figure. 6.12. PL spectra of nanoassemblies, methotrexate loaded nanoassembly and methotrexate.

In the chapter 5, we synthesized supramolecular architectures from LCDs with ester linking curcuminoids. They doesn't shows the emission peak in NIR region but introducing the imine linkage using APTES enhances its flourescence property and shows a fluorescence at higher emission wavelength extending in NIR region. The PL spectra of MTX loaded nanoassemblies (figure 6.12) shows the complete encapsulation of MTX, where the characteristic emission peak of MTX and nanoassemblies is disappeared and two new peaks are generated which extended to longer wavelength.

The drug loading capcity of nanoassemblies is found to be of 80 % and the encapsulation efficiency of MTX is found to be of 88 %. The introduction of imine linkage enhances the drug loading capacity compare to CL-LCDs reported in chapter 5. To model the *in vitro* MTX release behaviour in the typical physiological medium and the tumour intracellular medium, , the pH-triggered drug release from the proposed drug loaded nanoassemblies was carried out

at pH 7.4 PBS and pH 5.5 PBS respectively. In either of the two release profiles (figure 6.13), there was no discernible burst release.

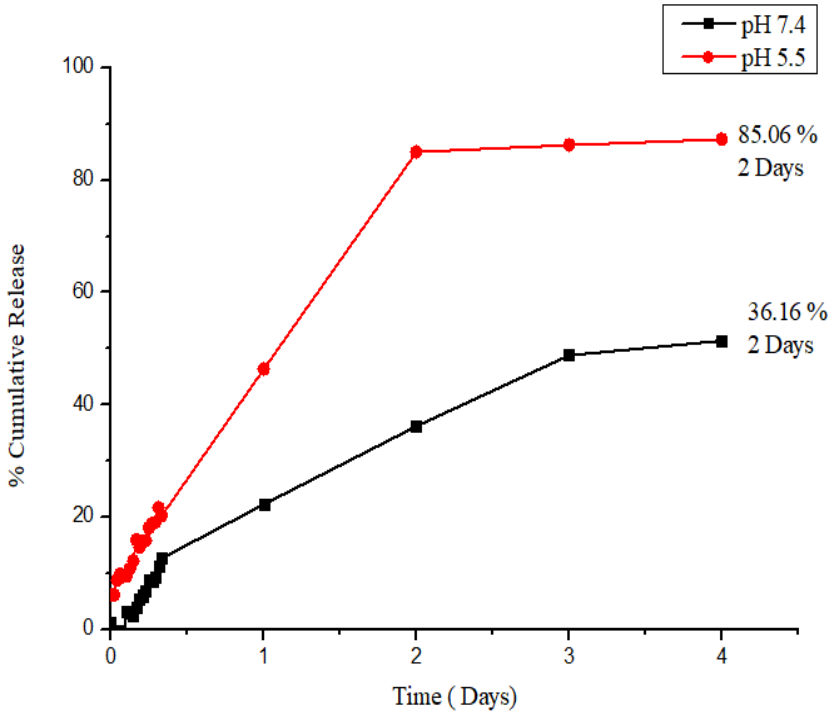

Figure. 6.13. *In vitro* release of MTX from the MTX ⊂ nanoassemblies.

It is anticipated that the toxic side effects of MTX on healthy cells and tissues would be reduced by the slow release of drug. The breakdown of the acid-sensitive -C=N bonds at pH 5.5, as in the weak acidic media simulating the tumour intracellular microenvironment, obviously sped up the drug release. In the first 24 hours, about 46.35% of the MTX could be released, and over the course of two days, the cumulative drug release increased to 85.06%.

The MTT assay on MCF-7 was used to assess the cytotoxicity of nanoassemblies, MTX loaded nanoassembly, and MTX in order to determine the efficacy of the prospective biomedical applications (Table. 6.1).

Sr. No.	**Compound**	**IC_{50} (MCF-7) (µg/ml)**
1.	Nanoassemblies	27.56 ± 1.2
2.	MTX ⊂ Nanoassemblies	18.43 ± 3.53
3.	MTX	20.19 ± 0.18

Table. 6.1 Cytotoxicity of nanoassemblies, MTX loaded nanoassemblies, and MTX against MCF-7 cancer cells for 24 hours incubation by MTT assay.

The cytotoxicity of free drug methotrexate and nanoassemblies was found to be comparable, with IC50 values of 20.19 µg/ml and 27.56 µg/ml, respectively. The cytotoxicity of nanoassemblies on MCF-7 cell line demonstrated the self-therapeutic properties of these entities (table 6.1). On MCF-7 cell line, the inclusion complex of nanoassemblies loaded with MTX had an IC50 value of 18.43 µg/ml. The preferential entry of MTX into malignant cells in the form of an inclusion complex is revealed by the improved cytotoxicity of inclusion complex compared to the free drug. In the instance of MCF-7 cells, the self-therapeutic effect of nanoassemblies may also be responsible for the synergistic cytotoxic effects of inclusion complex.

6.4. Conclusion

We synthesized APTES functionalized LCDs-NH_2 and reacted them with bis-aldehyde to generate an imine linked nanoassembles. The particle size of nanoassemblies was found to be 10 nm as revealed by HR-TEM images which is preferred for development of drug delivery system. The imine linkage in nanoassemblies shifts the emission to higher wavelength, indicating the potential application in the development of therenostic system. The drug loading and entrapement efficiency was found to be 80.01 % and 88.02 % which are better than the ester linked CDs (CL-LCDs). The nanoassemblies showed good sustained release of MTX under pH stimuli. 85.06 % of MTX was released in 2 days at pH 5.5. The investigation on cell viability using the MTT assay against the MCF-7 cell line demonstrated self-therapeutic behaviour of nanoassemblies and enhanced cytotoxic effect of inclusion complex.

6.5 Analytical Data

Spectrum 6.1: FT-IR spectrum of LCDs-NH_2

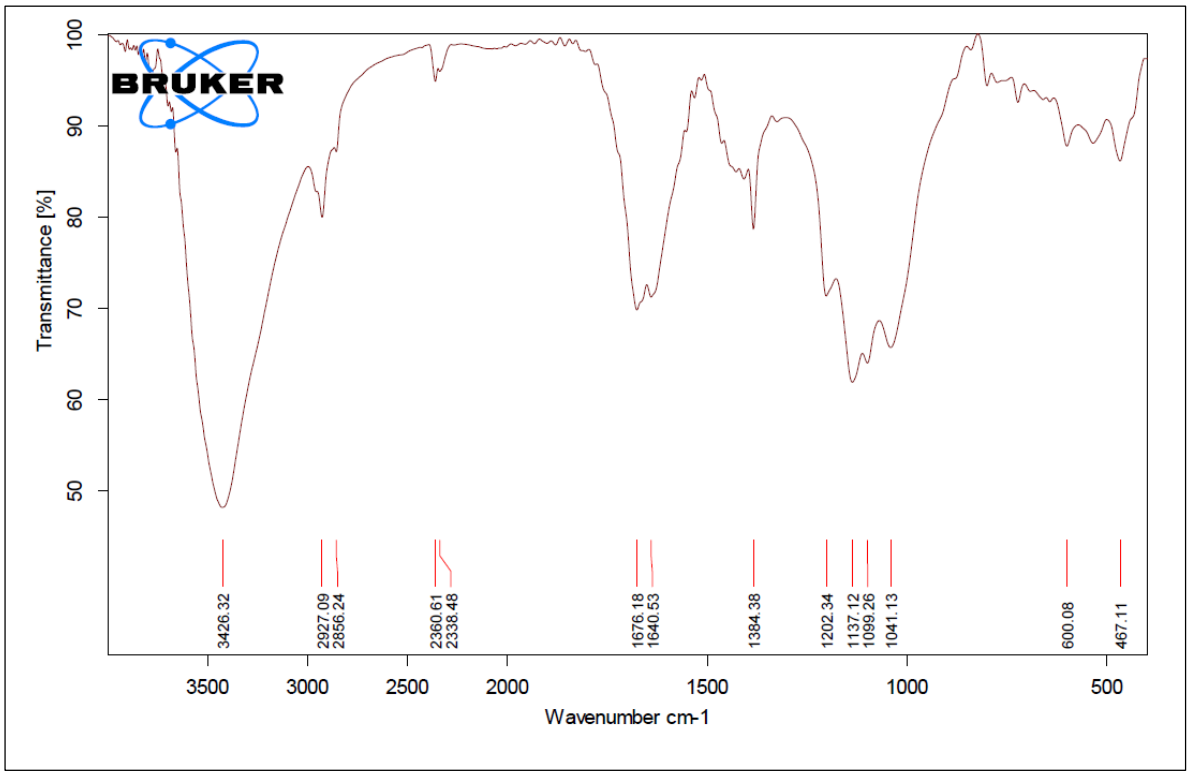

Spectrum 6.2: ^1H NMR spectrum of LCDs-NH_2 **DMSO-d_6**

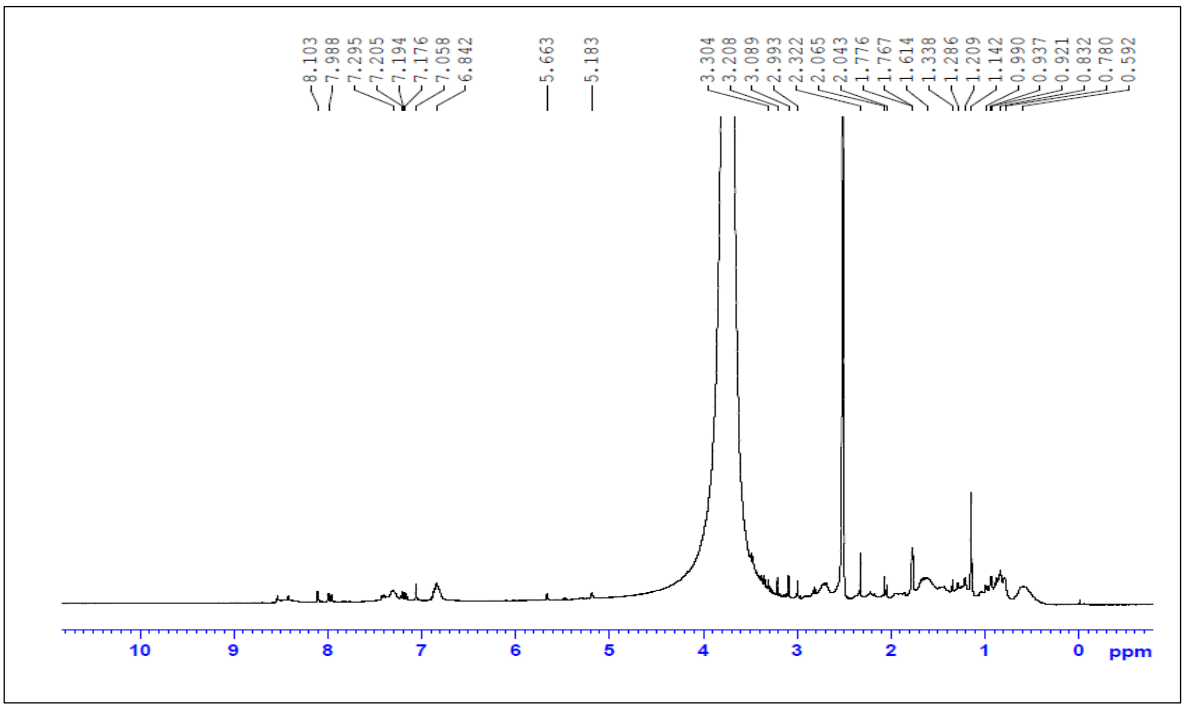

Spectrum 6.3: FT-IR spectrum of nanoassemblies

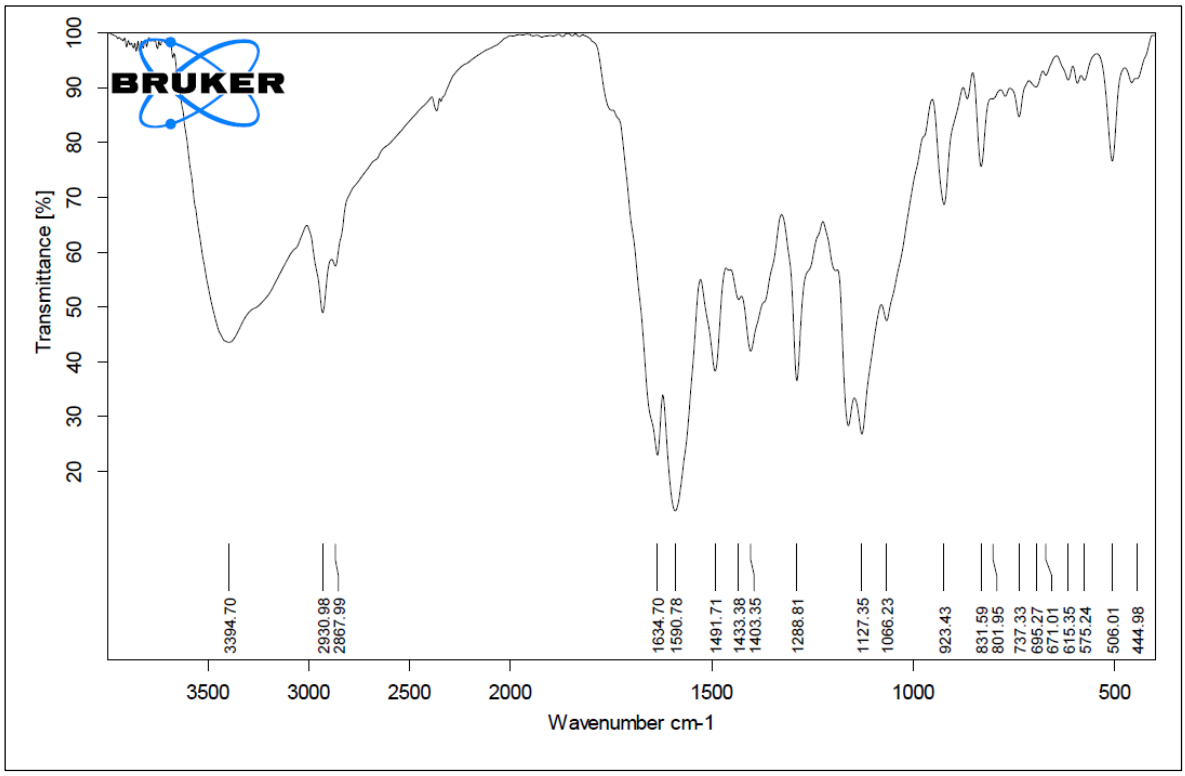

Spectrum 6.4: ^{1}H NMR spectrum of nanoassemblies

DMSO-d_6

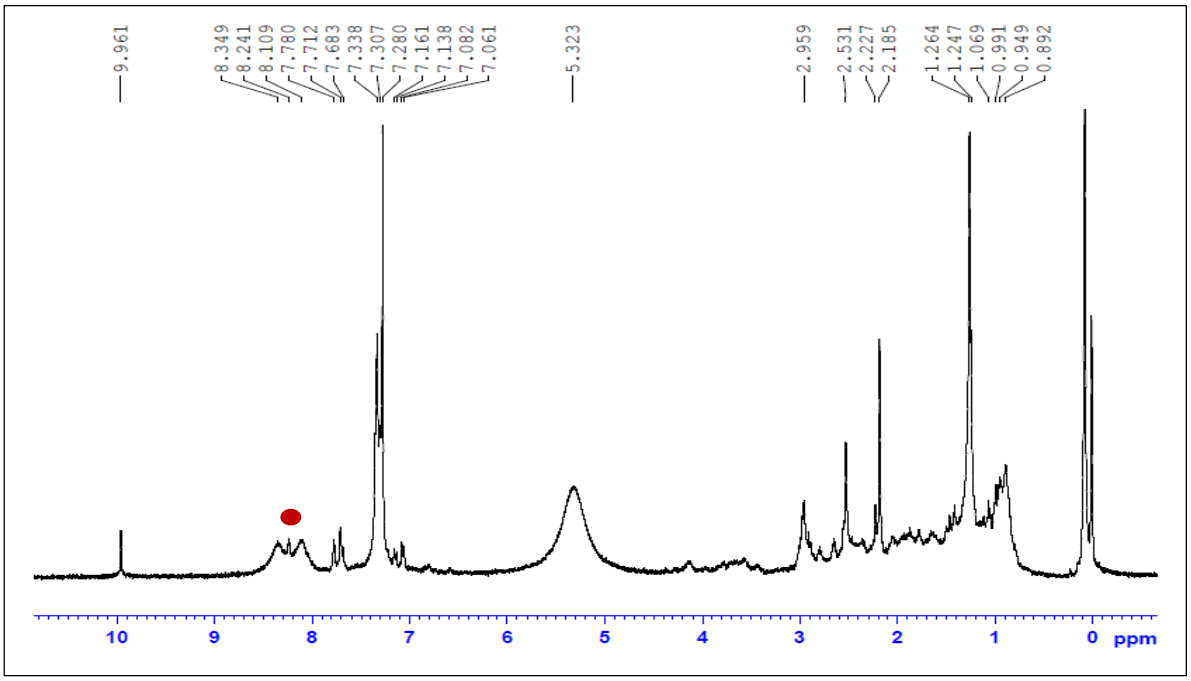

Spectrum 6.5: FT-IR spectrum of Methotrexate loaded nanoassemblies

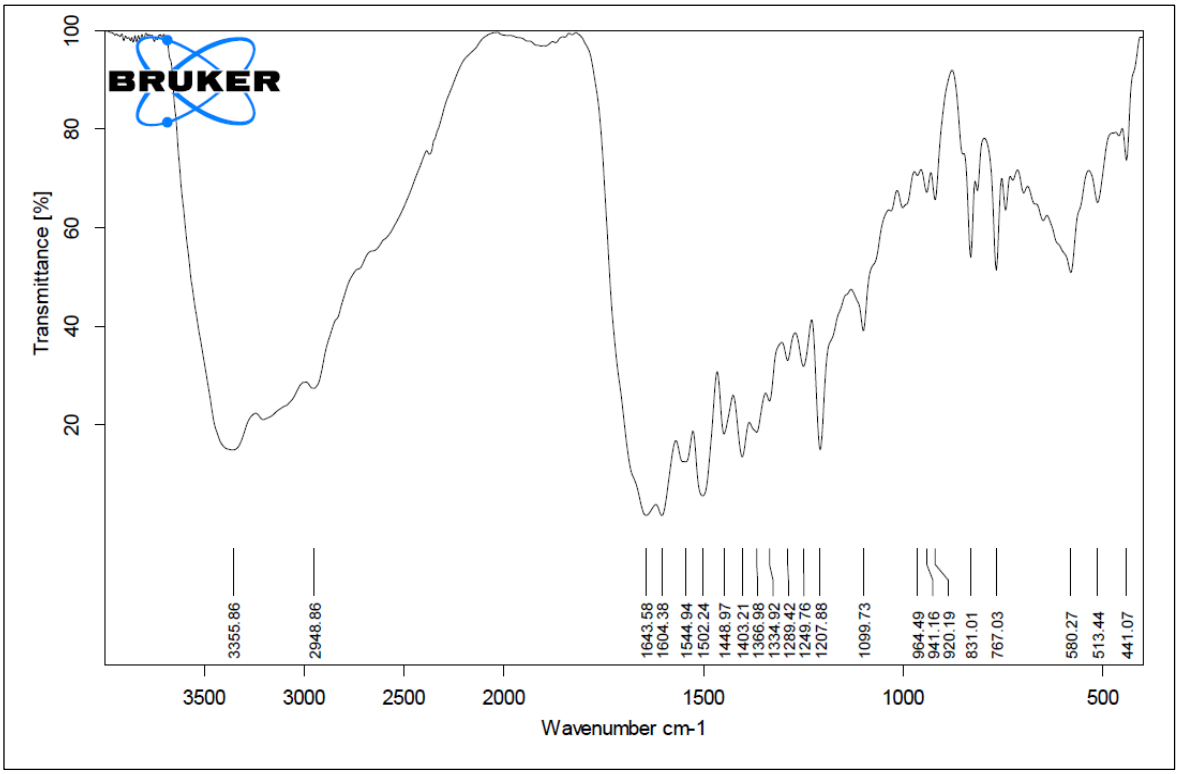

6.6. References

1 B. Kateb, K. Chiu, K. L. Black, V. Yamamoto, B. Khalsa, J. Y. Ljubimova, H. Ding, R. Patil, J. A. P. Arias, M. Modo, D. F. Moore, K. Farhani, M. S. Okun, N. Prakash, J. Neman, D. Ahdoot, W. Grundfest, S. Nikzad, J. D. Heiss, *Neuroimage*, 2011, **54**, S106-S124.

2 A. Topete, M. A. Meda, P. Iglesias, E. M. V. Alvarez, S. Barbosa, J. A. Costoya, P. Taboada, V. Mosquera, *ACS Nano*, 2014, **8**, 2725–2738.

3 Y. Zhang, Y. Shen, X. Teng, M. Yan, H. Bi, P. C. Morais, *ACS Appl. Mater. Interfaces*, 2015, **7**, 10201-10212.

4 Y. Cao, *EXPRESS Polym. Lett.*, 2018, **12**, 768-780 .

5 R. Sunasee, M. Carson, H. W. Despres, A. Pacherille, K. D. Nunez, K. Ckless, *J. Nanomater.*, 2019, **2019**, 1-9.

6 R. Sunasee, U. D. Hemraz, K. Ckless, *Expert Opin. Drug Deliv.*, 2016, **13**, 1243-1256.

7 C. Bharti, U. Nagaich, A. K. Pal, N. Gulati, *Int. J. Pharm. Investig.*, 2015, **5**, 124-133.

8 Y. Gao, D. Gao, J. Shen, Q. Wang, *Front. Chem.*, 2020, **8**, 1–17.

9 M. V. Regi, M. Colilla, I. I. Barba, M. Manzano, *Molecules*, 2018, **23**, 1–19.

10 S. K. Debnath, R. Srivastava, *Front. Nanotechnol.*, 2021, **3**, 1–22.

11 S. Zheng, Y. Tian, J. Ouyang, Y. Shen, X. Wang, J. Luan, *Front. Chem.*, 2022, **10**, 1–20.

12 H. Zare, S. Ahmadi, A. Ghasemi, M. Ghanbari, N. Rabiee, M. Bagherzadeh, M. Karimi, T. J. Webster, M. R. Hamblin, E. Mostafavi, I*nt. J. Nanomed.*, 2021, **16**, 1681–1706.

13 A. Mahor, P. P. Singh, P. Bharadwaj, N. Sharma, S. Yadav, J. M. Rosenholm, K. K. Bansal, *C*, 2021, **7**, 1-32.

14 E. Kianfar, *J. Supercond. Nov. Magn.*, 2021, **34**, 1709–1735.

15 P. M. Price, W. E. Mahmoud, A. A. Al-ghamdi, L. M. Bronstein, *Front. Chem.*, 2018, **6**, 1–7.

16 C. Comanescu, *Chemistry*, 2022, **4**, 872–930.

17 M. Kalubowilage, K. Janik, S. H. Bossmann, *Appl. Sci.*, 2019, **9**, 1-17.

18 G. M. Ziarani, M. Malmir, N. Lashgari, A. Badiei, *RSC Adv.*, 2019, **9**, 25094–25106.

19 T. Rodrigues, D. Reker, P. Schneider, G. Schneider, *Nat. Chem.*, 2016, **8**, 531-541.

20 A. Tyagi, K. M. Tripathi, N. Singh, S. Choudhary, R. K. Gupta, *RSC Adv.*, 2016, **6**, 72423–72432.

21 A. Kundu, S. Basu, B. Maity, *ACS Omega*, 2023, **8**, 36449-36459.

22 K. K. Gudimella, T. Appidi, H. Wu, V. Battula, A. Jogdand, A. Kumar, G. Gedda, *Colloid. Surf. B Biointerfaces*, 2021, **197**, 111362.

23 B. T. Hoan, P. D. Tam, V. Pham, *VNU J. Sci. Maths Phys.*, 2019, **35**, 62–69.

24 Y. Khor, A. R. A. Aziz, S. S. Chong, *Int. J. Nanoelectron. Mater.*, 2022, **15**, 241–253.

25 E. M. Schneider, A. Bartsch,W. J. Stark, R. N. Grass, *J. Chem. Edu.*, 2019, **96**, 540-545.

26 B. T. Hoan, P. D. Tam, V. H. Pham, *J. Nanotechnol.*, 2019, **2019**, 1-9.

27 H. Ding, Y. Ji, J. Wei, Q. Gao, Z. Zhou and H. Xiong, *J. Mater. Chem. B*, 2017, **5**, 5272-5277.

28 K. Merat, S. Ehsan, Z. Mostafa, *J. Adv. Biomed. Sci.*, 2022, **12**, 152–161.

29 M. He, J. Zhang, H. Wang, Y. Kong, Y. Xiao, W. Xu, *Nanoscale Res. Lett.*, 2018, **13**, 1-7.

30 A. Tadesse, M. Hagos, D. Ramadevi, K. Basavaiah, N. Belachew, *ACS Omega*, 2020, **5**, 3889-3898.

31 A. Tadesse, D. Ramadevi, M. Hagos, G. R. Battu, K. Basavaiah, *Asian J. Nanosci. Mater.*, 2018, **1**, 36–46.

32 J. Zhou, Z. Sheng, H. Han, M. Zou, C. Li, *Mater. Lett.*, 2012, **66**, 222–224.

33 C. Rodwihok, T. Van Tam, W. M. Choi, M. Suwannakaew, S. W. Woo, D. Wongratanaphisan, H. S. Kim, *Nanomaterials*, 2022, **12**, 1-13.

34 L. Han, P. Zhu, H. Liu, B. Sun, *Microchim. Acta*, 2022, **189**, 1–12.

35 S. Devi, R. K. Gupta, A. K. Paul, V. Kumar, A. Sachdev, P. Gopinath, S. Tyagi, *RSC Adv.*, 2018, **8**, 32684–32694.

36 P. G. Lou, F. Yang, S. T. Yang, S. K. Sonkar, L. Yang, J. J. Broglie, Y. Liu, Y. P. Sun, *RSC Adv.*, 2014, **4**, 10791–10807.

37 P. Dubey, K. M. Tripathi, R. Mishra, A. Bhati, A. Singh, S. K. Sonkar, *RSC Adv.*, 2015, **5**, 87528-87534.

38 K. M. Tripathi, A. K. Sonker, S. K. Sonkar, S. Sarkar, *RSC Adv.*, 2014, **4**, 30100–30107.

39 D. G. Babar, S. K. Sonkar, K. M. Tripathi, S. Sarkar, *J. Nanosci. Nanotechnol.*, 2014, **14**, 2334-2342.

40 J. Park, E. D. Grayfer, Y. Jung, K. Kim, K. K. Wang, Y. R. Kim, D. Yoon, H. Cheong, H. E. Chung, S. J. Choi, J. H. Choy, S. J. Kim, *J. Mater. Chem. B*, 2013, **1**, 1229-1234.

41 S. Devi, A. Kaur, S. Sarkar, S. Vohra, S. Tyagi, *Integr. Ferroelectr.*, 2018, **186**, 32–39.

42 X. T. Zheng, H. L. He, C. M. Li, *RSC Adv.*, 2013, **3**, 24853-24857.

43 S. Devi, R. K. Gupta, A. K. Paul, S. Tyagi, *Mater. Res. Express*, 2019, **6**, 1-12.

44 S. N. Baker, G. A. Baker, *Angew. Chem. Int. Ed.*, 2010, **49**, 6726–6744.

45 H. Liu, T. Ye, C. Mao, *Angew. Chem. Int. Ed.*, 2007, **46**, 6473–6475.

46 Y. Choi, S. Kim, M. Choi, S. Ryoo, J. Park, D. H. Min and B. S. Kim, *Adv. Funct. Mater.*, 2014, 1–9.

47 Y. Sun, B. Zhou, Y. Lin, W. Wang, K. A. S. Fernando, P. Pathak, M. J. Meziani, B. A. Harruff, X. Wang, H. Wang, P. G. Luo, H. Yang, M. E. Kose, B. Chen, L. M. Veca, S. Xie, *J. Am. Chem. Soc.*, 2006, **128**, 7756–7757.

48 J. Zhou, C. Booker, R. Li, X. Zhou, T. Sham, X. Sun, Z. Ding, *J. Am. Chem. Soc.*, 2007, **129**, 744–745.

49 L. Shen, L. Zhang, M. Chen, X. Chen, J. Wang, *Carbon N. Y.*, 2013, **55**, 343–349.

50 M. Zheng, Z. Xie, D. Qu, D. Li, P. Du, X. Jing, Z. Sun, *ACS Appl. Mater. Interfaces*,

2013, **5**, 13242-13247.

51 X. Lin, G. Gao, L. Zheng, Y. Chi, G. Chen, *Anal. Chem.*, 2014, **86**, 1223-1228.

52 J. Zong, Y. Zhu, X. Yang, J. Shen, C. Li, *Chem. Commun.*, 2011, **47**, 764–766.

53 L. Shi, J. H. Yang, H. B. Zeng, Y. M. Chen, S. C. Yang, C. Wu, H. Zeng, O. Yoshihito, Q. Zhang, *Nanoscale*, 2016, **8**, 14374-14378.

54 H. Wang, P. Gao, Y. Wang, J. Guo, K. Zhang, D. Du, X. Dai, G. Zou, *APL. Mater.*, 2015, **3**, 1-8.

55 L. Cao, M. J. Meziani, S. Sahu, Y. P. Sun, *Acc. Chem. Res.*, 2013, **46**, 171–180.

56 C. Fowley, B. Mccaughan, A. Devlin, I. Yildiz, F. M. Raymo, J. F. Callan, *Chem. Commun.*, 2012, **48**, 9361–9363.

57 Y. Dong, R. Wang, H. Li, J. Shao, Y. Chi, X. Lin, G. Chen, *Carbon*, 2012, **50**, 2810–2815.

58 Q. Q. Shi, Y. H. Li, Y. Xu, Y. Wang, X. B. Yin, X. W. He, Y. K. Zhang, *RSC Adv.*, 2014, **4**, 1563-1566.

59 W. Wang, Y. C. Lu, H. Huang, A. J. Wang, J. R. Chen, J. J. Feng, *Biosens. Bioelectron.*, 2015, **64**, 517–522.

60 S. Wang, I. S. Cole, D. Zhao, Q.Li, *Nanoscale*, 2016, **8**, 7449-7458.

61 H. Ding, S. B. Yu, J. S. Wei, H. M. Xiong, *ACS Nano*, 2016, **10**, 484-491.

62 A. Chemtob, L. Ni, C. Croutxø-barghorn, B. Boury, *Chem. Eur. J.*, 2014, **20**, 1790–1806.

63 D. K. Yi, S. T. Selvan, S. S. Lee, G. C. Papaefthymiou, D. Kundaliya, J. Y. Ying, *J. Am. Ahem. Soc.*, 2005, **127**, 4990–4991.

64 M. Zheng, Z. Xie, D. Qu, D. Li, P. Du, X. Jing, Z. Sun, *ACS Appl. Mater. Interfaces*, 2013, **5**, 13242-13247.

65 S. T. Selvan, P. K. Patra, C. Y. Ang, J. Y. Ying, *Angew. Chem. Int. Ed.*, 2007, **46**, 2448–2452.

66 A. Ulman, *Chem. Rev.*, 1996, **96**, 1533-1554..

67 Z. Zhelev, H. Ohba, R. Bakalova, *J. Am. Chem. Soc.*, 2006, **128**, 6324-6325.

68 S. R. Smith, J. J. Leitch, C. Zhou, J. Mirza, S. Li, X. Tian, Y. Huang, Z. Tian, J. Y. Baron, Y. Choi, J. Lipkowski, *Anal. Chem.*, 2015, **87**, 3791-3799.

69 R. M. Pasternack, S. R. Amy, Y. J. Chabal, *Langmuir*, 2008, **24**, 12963–12971.

70 X. Shao, H. Gu, Z. Wang, X. Chai, Y. Tian, G. Shi, *Anal. Chem.*, 2013, **85**, 418-425.

71 H. Rao, W. Liu, Z. Lu, Y. Wang, H. Ge, P. Zou, X. Wang, H. He, X. Zeng, Y. Wang, *Microchim. Acta*, 2016, **183**, 581–588.

72 W. Niu, D. Shan, R. Zhu, S. Deng, S. Cosnier, X. J. Zhang, *Carbon*, 2016, 96, 1034-1042.

73 Y. Lin, C. Wang, L. Li, H. Wang, K. Liu, K. Wang, B. Li, *ACS Appl. Mater. Interfaces*, 2015, **7**, 27262-27270.

74 G. Liu, Z. Chen, X. Jiang, D. Q. Feng, J. Zhao, D. Fan,W. Wang, *Sensors Actuators B. Chem.*, 2016, **228**, 302-307.

75 J. Yang, Z. Z. Lin, A. Z. Nur, Y. Lu, M. H. Wu, J. Zeng, X. M. Chen, Z. Y. Huang, *Spectrochim. Acta-A: Mol. Biomol. Spectrosc.*, 2018, **190**, 450-456.

76 M. S. Kang, R. K. Singh, T. Kim, J. Kim, D. Kapil and H. Kim, *Acta Biomater.*, 2017, **55**, 466-480.

77 M. P. Shirani, B. Rezaei, T. Khayamian, M. Dinari, F. Hosseini, M. Ramezani and M. Alibolandi, *Mater. Sci. Eng. C*, 2018, **92**, 892–901.

78 A. B. Siddique, A. K. Pramanick, S. Chatterjee, M. Ray, *Sci. Rep.*, 2018, **8**, 1–10.

79 B. T. Hoan, P. D. Tam, V. H. Pham, *J. Nanotechnol.*, 2019, **2019**, 1-9.

80 L. Li, T. Dong, *J. Mater. Chem. C*, 2018, **6**, 7944-7970.

81 F. Yan, Y. Jiang, X. Sun, Z. Bai, Y. Zhang, X. Zhou, *Microchim. Acta*, 2018, **185**, 1-34.

82 B. De, N. Karak, *RSC Adv.*, 2013, **3**, 8286-8290.